



Adaptation of an unstructured-mesh, finite-element ocean model to the simulation of ocean circulation beneath ice shelves

Satoshi Kimura^{a,b,*}, Adam S. Candy^b, Paul R. Holland^a, Matthew D. Piggott^{b,c}, Adrian Jenkins^a

^a British Antarctic Survey, High Cross Madingley Road, Cambridge CB3 0ET, UK

^b Applied Modelling and Computation Group, Department of Earth Science and Engineering, Imperial College London, South Kensington Campus, London SW7 2AZ, UK

^c Grantham Institute for Climate Change, Imperial College London, South Kensington Campus, London SW7 2AZ, UK

ARTICLE INFO

Article history:

Received 17 October 2012

Received in revised form 25 February 2013

Accepted 22 March 2013

Available online 12 April 2013

Keywords:

Ice shelf

Ice–ocean interaction

Unstructured mesh

Fluidity-ICOM

ABSTRACT

Several different classes of ocean model are capable of representing floating glacial ice shelves. We describe the incorporation of ice shelves into Fluidity-ICOM, a nonhydrostatic finite-element ocean model with the capacity to utilize meshes that are unstructured and adaptive in three dimensions. This geometric flexibility offers several advantages over previous approaches. The model represents melting and freezing on all ice-shelf surfaces including vertical faces, treats the ice shelf topography as continuous rather than stepped, and does not require any smoothing of the ice topography or any of the additional parameterisations of the ocean mixed layer used in isopycnal or z-coordinate models. The model can also represent a water column that decreases to zero thickness at the ‘grounding line’, where the floating ice shelf is joined to its tributary ice streams. The model is applied to idealised ice-shelf geometries in order to demonstrate these capabilities. In these simple experiments, arbitrarily coarsening the mesh outside the ice-shelf cavity has little effect on the ice-shelf melt rate, while the mesh resolution within the cavity is found to be highly influential. Smoothing the vertical ice front results in faster flow along the smoothed ice front, allowing greater exchange with the ocean than in simulations with a realistic ice front. A vanishing water-column thickness at the grounding line has little effect in the simulations studied. We also investigate the response of ice shelf basal melting to variations in deep water temperature in the presence of salt stratification.

© 2013 Elsevier Ltd. All rights reserved.

1. Introduction

Satellite observations suggest that the mass loss of the Antarctic and Greenland ice sheets is accelerating with time (Rignot and Kanagaratham, 2006; Velicogna, 2009). The most profound changes in ice-sheet thickness are observed near ocean margins (Pritchard et al., 2009); commonly assumed to be caused by increased melting at the margin termini. In colder areas of Greenland and Antarctica, ice streams flow out over the ocean to form large floating ice shelves. The point at which the ice starts to float is called the ‘grounding line’ and the iceberg-calving edge at the ocean end of ice shelves is called the ‘ice front’.

Exchange of heat and salt at the ice–ocean interface can drive a large-scale oceanic circulation beneath ice shelves. Under the larger Antarctic ice shelves such as Filchner–Ronne and Ross, a cold (−1.9 °C) and dense water mass known as High Salinity Shelf Water (HSSW), generated by brine rejection from sea ice formation on the continental shelf, enters beneath the ice shelves (Nicholls

and Østerhus, 2004; Nicholls et al., 2009). As a result of the decrease in the freezing temperature with depth, this HSSW melts the base of the ice shelves, producing cold and fresh buoyant meltwater that retains its temperature below the surface freezing point (Jacobs et al., 1979; Smethie and Jacobs, 2005). As this plume of meltwater ascends along the ice base, it becomes supercooled, owing to the increase in situ freezing temperature with the falling pressure, and freezes onto the ice base (Jacobs et al., 1992; Jenkins and Bombosch, 1995; Holland and Feltham, 2006). The properties of the HSSW are constrained by brine rejection at the sea surface freezing temperature, so the HSSW intruding to these large ice shelves cannot increase in temperature significantly (MacAyeal, 1984).

In contrast, smaller West Antarctic ice shelves in the Amundsen and Bellingshausen Seas, such as Pine Island Glacier and George VI Ice Shelf, can be susceptible to changes in the warm (+1 °C) Circumpolar Deep Water (CDW) that floods the continental shelf (Jacobs et al., 1996). Modelling work of Thoma et al. (2008) suggested that the variability in the westerly wind stress near the continental shelf edge could drive changes in the CDW inflow onto the Amundsen sea shelf. Steig et al. (2012) argue that changes in the wind forcing are associated with anomalous high sea-level pressure to

* Corresponding author at: British Antarctic Survey, High Cross Madingley Road, Cambridge CB3 0ET, UK. Tel.: +44 (0)1223 221317.

E-mail address: satmur65@bas.ac.uk (S. Kimura).

the north of the Amundsen Sea and an increase in sea surface temperature in the central tropical Pacific. Upper water column properties at the Pine Island Glacier front are characterized by a mixture of the CDW and meltwater (Jenkins, 1999), indicating that intrusions of CDW beneath the ice shelf are responsible for its high melt rate (Jenkins et al., 1997; Jacobs et al., 1996; Shepherd et al., 2004). This idea is confirmed by direct observations of temperature, salinity and dissolved oxygen beneath the Pine Island Glacier using an autonomous underwater vehicle (Jenkins et al., 2010). These observations show that CDW with a temperature several degrees above the in situ freezing point floods the cavity, enabling ice to melt in excess of 50 m yr^{-1} .

There have been many efforts to explicitly represent ice shelf cavities in ocean models. These ocean models employ either terrain-following (σ), z , or isopycnal coordinates. The σ -coordinate models provide a convenient framework to represent ice shelf cavities by subducting the surface layer to follow the ice topography (Determann and Gerdes, 1994; Grosfeld et al., 1997; Beckmann et al., 1999; Dinniman et al., 2007). A potential advantage is that narrowing of the water column results in high vertical resolution near the grounding line, but this requires a minimum water-column thickness to be imposed to prevent the coordinate surfaces converging. Another advantage of this approach is that ice–ocean interactions can be applied along the subducted surface layer, providing a smoothly-varying melt rate consistent with the prognostic variables used to calculate the melt rate. However, σ -coordinate models are prone to spurious motions caused by truncation errors in the horizontal pressure gradients near steep topography (e.g. Gary, 1973; Haney, 1991; Mellor et al., 1994). Spurious motions can be reduced by either increasing the grid resolution or smoothing topography. This is particularly important near the ice front, where a step-change in water column thickness of several hundreds of metres is expected. The problems with σ -coordinate models at ice fronts are commonly overcome by smoothing the topographic step between the ice shelf cavity and the open ocean (Beckmann et al., 1999).

Losch (2008) incorporated ice shelves into a z -coordinate ocean model (MITgcm). This coordinate system is not a natural choice for modelling ice-shelf cavities but can have great benefits elsewhere, so it is important that ice shelves can be represented within the model framework. One problem is that z -coordinate models represent the ice base as a step-like feature, leading to discontinuities in the temperature, salinity, and velocity fields that then cause striped artefacts to appear in the melt rate. This problem can be largely mitigated by using partial cells (Adcroft et al., 1997) to represent the boundary and by using a boundary layer parameterisation to provide ocean fields to calculate the melt rate and receive the meltwater flux in return (Losch, 2008). Another fundamental problem is that resolving processes in the ice-shelf cavity requires high vertical resolution. Since a z -coordinate model must have vertical resolution that is horizontally uniform, this implies a waste of computational resources outside the cavity, in areas that could otherwise be very coarsely represented.

Isopycnal coordinate models can achieve a smooth representation of the ice base and do not suffer from pressure-gradient errors, and can efficiently represent the cavity circulation alongside the open ocean if the density range is similar between the two (Holland and Jenkins, 2001; Little et al., 2008). Isopycnal coordinates are also a natural choice for accurately introducing the pressure forcing exerted by a floating ice shelf to the ocean. The model calculates the evolution of the pressure difference between isopycnals, rather than determining the varying pressure at fixed positions, which is required by the other approaches. One disadvantage of this approach is the need to choose the isopycnal layers carefully in order to resolve the features of interest; in the case of ice shelves this may require a choice that is sub-optimal for the rest of the ocean. In addition, the

interaction between the isopycnal ocean interior and ice shelf or atmosphere is typically handled using a non-isopycnal mixed layer parameterisation, which implies several assumptions about the nature of turbulence at the ice shelf/ocean interface. This parameterisation is particularly troublesome at ice shelf fronts, where the sub-ice shelf mixed layer must somehow join the open-ocean surface mixed layer (Holland and Jenkins, 2001).

Many of these models have been applied to understand the ocean circulation beneath relatively large ice shelves ($\sim 500 \text{ km}$ in shelf length), such as Filchner–Ronne, Amery and Ross ice shelves (e.g. Grosfeld et al., 1997; Williams et al., 1998; Beckmann et al., 1999; Jenkins and Holland, 2002; Dinniman et al., 2007; Losch, 2008; Makinson et al., 2011). Our aim is to develop a model that can contribute to the understanding of recent observations of rapid melting of smaller ice shelves in Greenland and Antarctica, which have lengths of $\sim 50 \text{ km}$ (e.g. Rignot and Steffen, 2008; Holland et al., 2008a; Straneo et al., 2010; Jenkins et al., 2010). In these smaller domains, the ice shelf and seabed morphology can be quite complicated. For example, Rignot and Steffen (2008) reported inverted channels beneath the ice shelf of Petermann Glacier in northwest Greenland, and similar features were observed in Pine Island Glacier (Jenkins et al., 2010). Representing these features accurately in the ocean models described above is computationally demanding and their effect on basal melting is largely unknown.

The use of the finite-element method and an unstructured mesh has great advantages in resolving both small and large scale ocean flows while smoothly varying the resolution and conforming to complex coastlines and bathymetry (e.g. Lynch et al., 1996; Danilov et al., 2004; Timmermann et al., 2009). Timmermann et al., 2012 incorporated ice shelves into a finite-element, horizontally-unstructured-mesh ocean model with the use of a hybrid coordinate system in the vertical. The hybrid coordinate system employs the σ -coordinate system in ice-shelf cavities and the z -coordinate system in the open ocean. While the use of horizontally-unstructured mesh can adequately represent the coastlines, this approach still suffers from the disadvantages of the σ -coordinate system in representing ice shelf cavities.

In this study, we incorporate ice shelves into a nonhydrostatic, finite-element fully-unstructured-mesh ocean model (Fluidity-ICOM). The fully-unstructured-mesh does not constrain the location of nodes in the ice shelf cavity as in z - or σ -coordinate models. The intention of this study is to demonstrate the basic abilities of the model, and test the effect of some of its improvements over previous approaches. A full incorporation of ice-shelf pressure loading, applications to realistic complex topography, and the use of adaptive meshing techniques will not be discussed in this paper. The model is described in Section 2. Section 3 describes our base case. The effects of using different types of unstructured mesh are examined in Section 4. Section 5 explores the effects of domain geometry on the circulation of meltwater. The sensitivity of melt rate to various thermal forcings is examined in Section 6. Finally, our conclusions are summarised in Section 7.

2. Model description

The Boussinesq equations are cast in a rotating Cartesian coordinate system $\{x, y, z\}$ with the rotation vector $\Omega = \{0, 0, \Omega_z\}$, where we used $\Omega_z = -5 \times 10^{-5} \text{ s}^{-1}$, equivalent to $\sim 70^\circ \text{S}$. Buoyancy is assumed to be a linear function of the temperature and salinity. The resulting field equations describing the time evolution of the instantaneous velocity field $\vec{u}(x, y, z, t) = \{u, v, w\}$, the temperature, T and the salinity, S are

$$\frac{D\vec{u}}{Dt} + 2\Omega \times \vec{u} = -\frac{1}{\rho_0} \nabla P + b\hat{k} + K_H \nabla_H^2 \vec{u} + K_z \frac{\partial^2 \vec{u}}{\partial z^2}; \quad (1)$$

$$\nabla \cdot \vec{u} = 0; \quad (2)$$

$$\frac{DT}{Dt} = K_H \nabla_H^2 T + K_z \frac{\partial^2 T}{\partial z^2}; \quad (3)$$

$$\frac{DS}{Dt} = K_H \nabla_H^2 S + K_z \frac{\partial^2 S}{\partial z^2}. \quad (4)$$

The variables ρ_0 and P represent the reference density and pressure. The horizontal and vertical diffusion of momentum, temperature and salinity are represented by K_H and K_z , respectively. Here, we assume $K_H = 100 \text{ m}^2 \text{ s}^{-1}$ and $K_z = 10^{-5} \text{ m}^2 \text{ s}^{-1}$. The horizontal Laplacian operator, $\partial^2/\partial x^2 + \partial^2/\partial y^2$ is represented by ∇_H^2 . The buoyancy force $b = -g(-\alpha(T - T_0) + \beta(S - S_0))$ is parallel to the vertical unit vector, k , and g is the acceleration due to gravity. The constants T_0 and S_0 are reference values of temperature and salinity and α and β are the coefficients of thermal expansion and saline contraction respectively. According to our choice of $T_0 = 1^\circ \text{C}$ and $S_0 = 35 \text{ PSU}$, α and β are set to $10^{-4} \text{ }^\circ\text{C}^{-1}$ and $7.6 \times 10^{-4} \text{ PSU}^{-1}$, respectively. While the nonlinearity of the equation of state can be important in the polar regions, we do not expect it to play a critical role in these experiments; since, changes in temperature are directly associated with changes in salinity that dominates the buoyancy forcing. In future studies, we will represent the equation of state using an algorithm described in McDougall et al. (2003).

We utilize finite-element discretisation methods implemented in Fluidity-ICOM (Piggott et al., 2008) to solve (1)–(4). Velocity and pressure are discretised within first-order discontinuous and second-order continuous function spaces (a $P1_{DG} - P2$ finite element pair), as described in Cotter et al. (2009). This element pair allows us to represent the discrete geostrophic balance exactly, and is appropriate for modelling large-scale ocean dynamics. The pressure is solved according to the procedure described in Kramer et al. (2009). The nodes in our meshes are aligned vertically to minimize the separation between horizontal (barotropic) and vertical modes in the pressure equation. Scalar equations are discretised using $P1_{DG}$. An implicit time stepping scheme is used for advancing the prognostic variables in time, with a time step of 200 s.

While the $P1_{DG} - P2$ formulation can solve the equations on an unstructured mesh which cannot generally be done with other ocean models, it comes with an increase in computational overhead. Because the representation of velocity is allowed to be discontinuous, there are more degrees of freedom than other models for a given horizontal and vertical mesh spacing. Also, since the connectivity of neighbouring elements is an arbitrary choice in unstructured meshes, the central processing unit (CPU) needs to load the information of the neighbouring elements from the main memory every time they are required, which can increase the information traffic between the CPU and main memory and slow down the simulation.

2.1. Ice shelf parameterization

This study presents simulations performed with a ‘rigid lid’, in which the location of the ice shelf and open ocean surface are fixed, but their surface experiences a variable pressure according to the predicted dynamics. Under these conditions, the task of introducing ice shelves reduces to applying thermodynamic boundary conditions at the ice–ocean interface.

The temperature T_b at the ice–ocean interface is at the local freezing temperature determined by the salinity S_b at the ice–ocean interface:

$$T_b = aS_b + b + cP, \quad (5)$$

where $a = -0.0573 \text{ }^\circ\text{C}$, $b = 0.0832 \text{ }^\circ\text{C}$ and $c = -7.53 \times 10^{-8} \text{ }^\circ\text{C Pa}^{-1}$. The local freezing relation is linked with the balance of heat and salt

fluxes between the ice and ocean (McPhee, 2008; Jenkins and Bombosch, 1995):

$$m'L + m'c_l(T_b - T_l) = c_0\gamma_T u_\infty(T_\infty - T_b); \quad (6)$$

$$m'S_b = \gamma_S u_\infty(S_\infty - S_b), \quad (7)$$

where $c_0 = 3974 \text{ J kg}^{-1} \text{ }^\circ\text{C}^{-1}$ and $c_l = 2009 \text{ J kg}^{-1} \text{ }^\circ\text{C}^{-1}$ are the specific heat capacity of seawater and ice, respectively. The velocity of the ocean in the direction normal to the ice–ocean interface is represented by m' and the melt rate of ice is $m = \rho_w m' / \rho_{ice}$, where ρ_w and ρ_{ice} are the density of the ocean and ice, respectively. The variable $L = 3.35 \times 10^5 \text{ J kg}^{-1}$ represents the latent heat of ice fusion. Non-dimensional coefficients of the heat and salt transfer through the boundary layer are represented by γ_T and γ_S , where these numbers are a function of the molecular Prandtl number (the ratio of viscosity to thermal diffusivity) and Schmidt number (the ratio of viscosity to saline diffusivity), respectively (Holland and Jenkins, 1999). According to their formula, we have assumed $\gamma_T = 1.05 \times 10^{-3}$ and $\gamma_S = 3.97 \times 10^{-5}$. These values are independent of the thickness of the ice–ocean boundary layer, since they are scaled with the far-field velocity.

The far-field internal temperature of ice is assumed to be $T_l = -25^\circ \text{C}$. The terms on the right-hand sides of (6) and (7) are a parameterisation of the mixing of heat and salt towards the ice through the oceanic boundary layer. The far-field ocean temperature and salinity are represented by T_∞ and S_∞ . The variable u_∞ represents the speed of ocean flow oriented parallel to the ice shelf, which is taken to be the source of turbulence that drives the mixing of heat and salt towards the ice. The resulting heat and salt fluxes to the ocean are calculated according to Jenkins et al. (2001):

$$F_H = c_0(\gamma_T u_\infty + m')(T_\infty - T_b); \quad (8)$$

$$F_S = (\gamma_S u_\infty + m')(S_\infty - S_b). \quad (9)$$

The three unknowns, T_b , S_b , and m' , are solved by combining (5)–(7) to produce a quadratic equation, of which one solution of S_b is positive definite (e.g. Hellmer and Olbers, 1989; Holland and Jenkins, 2001; Losch, 2008). This approach is applied to calculate a melt rate on any element boundary surface that is defined to be ice, regardless of its orientation.

Previous approaches usually take the far-field values at a distance from the ice that varies over the ice surface. For instance, σ -coordinate models usually use values from the top layer beneath the ice, while isopycnic- and z -coordinate models take values from mixed-layer parameterisations. All finite-difference or – volume models produce a step-like representation of the sub-ice boundary layer that is not optimal in resolving its gradients. In a finite element approach, the values vary within elements according to the choice of basis function (here discontinuous linear for velocity and scalars). We are therefore free to choose any location for the far-field values; meaningful values are obtained at any point irrespective of the mesh chosen. In this study, we choose to define a far-field surface that is parallel to the ice–ocean interface. The distance between the far-field surface and ice–ocean interface is the thickness of the ocean boundary layer, which we here assume to be 1 m. One drawback of this approach is that for a small fraction of ice surfaces the far-field surface can be located outside of the computational domain (e.g. when the water column is less than 1 m thick). In this case, the thickness of the ocean boundary layer is successively decreased until the far-field surface resides inside the computational domain.

2.2. Numerical experiments

Our computational domain is represented by tetrahedral elements. Each tetrahedron is composed of four nodes and faces. By

changing the distribution of nodes (mesh), we can vary the spatial resolution, and the use of unstructured meshes theoretically implies total freedom in the placement of nodes. The only restriction is that nodes must be vertically aligned to expedite the pressure scheme.

We consider four different types of horizontal mesh (Fig. 1) and four different types of vertical mesh (Fig. 2). The horizontal mesh H_1 employs a structured mesh, where nodes of tetrahedral elements are aligned in the x and y directions with a uniform spacing of 1 km (Fig. 1(a)). The other three horizontal meshes utilise unstructured meshes in which each node is separated by a horizontal characteristic length. The H_2 mesh has a spatially uniform characteristic length of 1 km (Fig. 1(b)). The meshes H_3 and H_4 have 1 km characteristic length inside the ice shelf cavity and the characteristic length linearly increases to 5 and 10 km toward the northern boundary in the open-ocean portion, respectively (Fig. 1(c) and (d)). These meshes are generated by Gmsh described in Geuzaine and Remacle (2009).

To keep the nodes aligned in the vertical direction, each of these horizontal meshes is vertically extruded to form a three-dimensional idealized domain containing a 50 km long ice shelf cavity inside a 100 km long ocean. We consider two different types of extrusion: quasi- σ and quasi- z coordinate systems. The number of vertical layers (n) is fixed in the quasi- σ coordinate system, (e.g. Fig. 2(a) and (b)), in which extra layers are added outside the ice-shelf cavity to resolve the ice front better (as implemented by Grosfeld et al. (1997)). Unlike conventional σ -coordinate systems, our quasi- σ is capable of collapsing vertical layers to a single point, representing the grounding line (Fig. 2(a)). Ten internal layers are used to represent the open ocean with a vertical spacing of 100 m. The layers $n = 0$ and $n = 9$ represent the surface and bottom of the ocean respectively. The bottom 8 layers, $n = 2$ – 9 , extend

to the ice shelf cavity, and these layers are collapsed to a single point at the grounding line. In the case of non-zero grounding line, one extra layer is added at the bottom of the open ocean, and the water column thickness at the grounding line is 100 m (Fig. 2(b)).

A 'target' vertical spacing (dz) is specified in the quasi- z coordinate system. The meshes, V_2 and V_3 , have dz of 100 m and 50 m, respectively (Fig. 2(c) and (d)). The water column thickness in the ice-shelf cavity is not necessarily an integer multiple of dz , so strictly applying dz would result in the need to accommodate an oddly sized element somewhere in the water column. Instead, the vertical locations of the nodes are chosen by evenly splitting the remainder of the water column thickness and adding it to each vertical layer. Therefore, the vertical nodes are not horizontally aligned as in the conventional z -coordinate system. As the dz becomes smaller, the quasi- z coordinate system becomes more like the conventional z coordinate system (Fig. 2(c) and (d)) because the number of elements that accommodate the remainder increases, decreasing the deviation from the 'target' vertical spacing, dz .

We consider combinations of two salinity and six temperature profiles for initial conditions (see Fig. 3). At the northern boundary, the ocean conditions are restored back to these initial conditions on time scales increasing linearly with distance from the boundary between 10 days ($y = 100$ km) and 30 days ($y = 90$ km). The uniform salinity and temperature profiles, S_1 and T_1 , are used in most simulations in order to simply visualise the ice-shelf meltwater (Table 1). The other profiles are a reasonable generalization of the continental shelf waters surrounding most of Antarctica, where cool, fresh water masses overlay warm, salty water, and are used in an attempt to reproduce the results of Holland et al. (2008b). These profiles are employed to examine the response of melt rate to thermal forcing (Table 2).

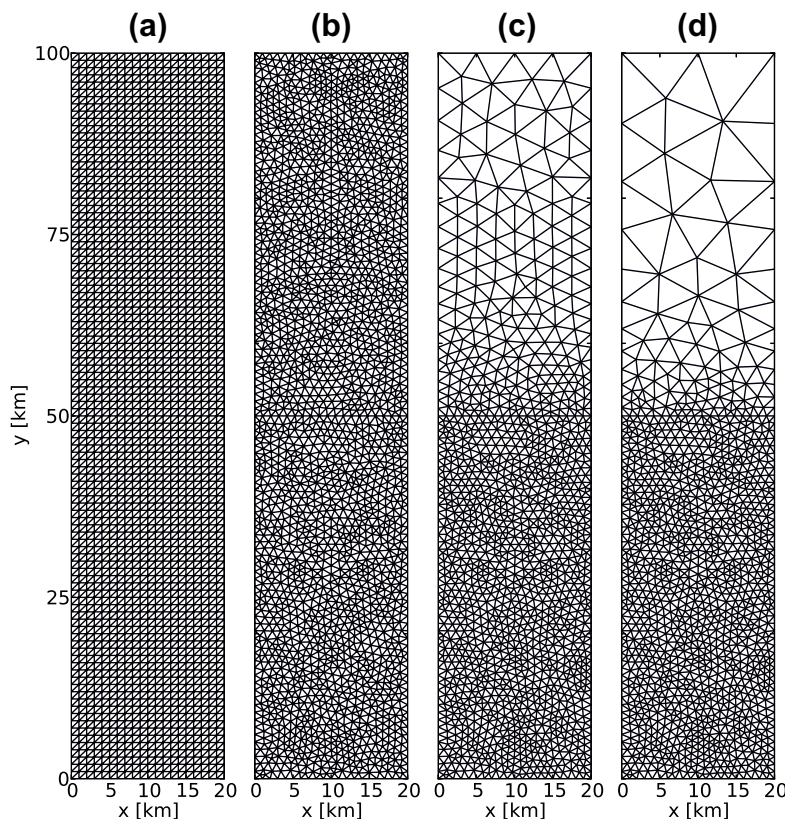


Fig. 1. Four different horizontal meshes: (a) H_1 , (b) H_2 , (c) H_3 , and (d) H_4 . The ice shelf front is located at $y = 50$ km. The meshes H_2 , H_3 and H_4 are used in $dr = 1$ km, $dr = 5$ km and $dr = 10$ km. The rest of the numerical experiments uses H_1 .

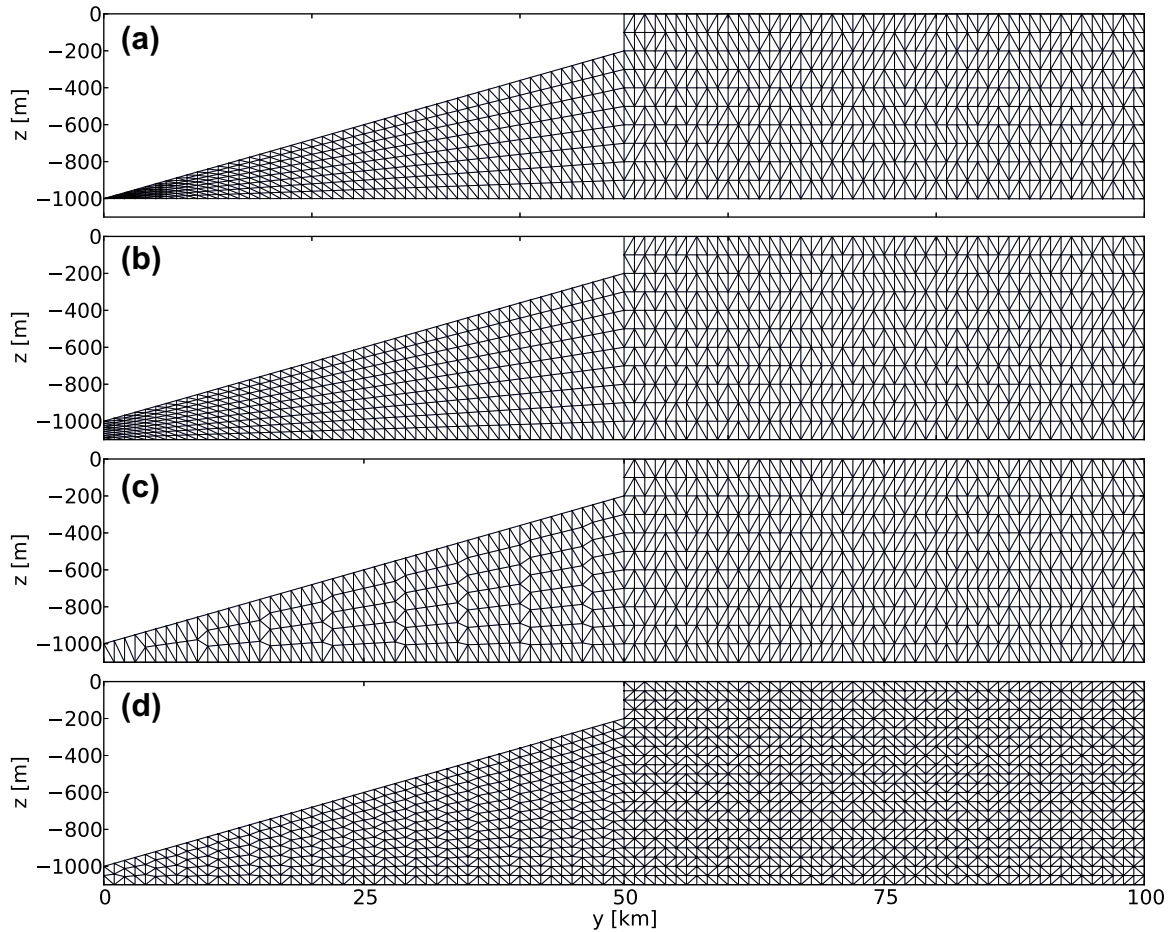


Fig. 2. Different types of vertical mesh: (a) quasi- σ with zero thickness grounding line, (b) V_1 , quasi- σ with the water depth of 100 m at the grounding line, (c) V_2 , quasi- σ with $dz = 100$ m and (d) V_3 , quasi- z with $dz = 50$ m. Exchanges of heat and salt are applied along the ice–ocean interface, composed of an ice shelf base and ice shelf front. The ice shelf base extends from $(y, z) = (0, -1000)$ m to $(y, z) = (50, -200)$ m. A vertical ice shelf front of 200 m depth is located at $y = 50$ km.

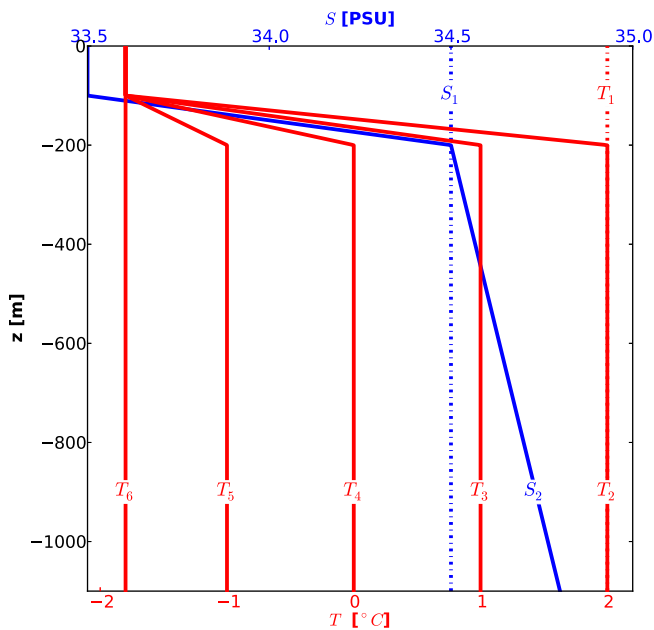


Fig. 3. Initial profiles of salinity and temperature. The profiles, S_1 and T_1 have vertically uniform salinity and temperature of 34.5 PSU and 2 °C. The rest of the profiles have vertically varying salinity and temperature as used in Holland et al. (2008b). These profiles are used in simulations described in Section 6.

Zero-flux temperature and salinity boundary conditions are applied at all the boundaries except at the ice–ocean interface. For velocity boundary conditions we apply quadratic drag with a drag coefficient of 0.0025 along all the boundaries except the Northern one, where a free-slip boundary condition is applied. All the boundary conditions are applied with respect to the discretized function space in which solutions are approximated, i.e., the boundary conditions are applied in a weak form. Our idealized experiments do not have surface buoyancy forcing. In reality, surface buoyancy force can be important in regulating inflow of the open-ocean, thereby changing the melt rate.

3. Base case

Under the individual conditions introduced above, the large-scale circulation beneath an ice shelf is dominated by the production of meltwater caused by the exchanges of heat and salt at the ice–ocean interface. In a model development study such as this, it is important to make sure that the change in water masses is generated correctly by the melting of ice. The simplest way to track the meltwater is to examine the water property evolution relative to a temperature and salinity relationship described by the theory of Gade (1979). This theory dictates that any water mass with T and S , generated by the melting of glacial ice, should lie on a straight line that passes through T_s and S_s in temperature–salinity space:

$$T = \frac{T_s - T_f + L/c_0 + (c_l/c_0)(T_f - T_l)}{S_s} (S - S_s) + T_s, \quad (10)$$

Table 1

Experiments described in Sections 3 and 4 for different types of mesh. The variable dr represent the characteristic length of the mesh in the horizontal directions.

Case	Base case	$dr = 1$ km	$dr = 5$ km	$dr = 10$ km	$dz = 100$ m	$dz = 50$ m
Horizontal mesh	H_1	H_2	H_3	H_4	H_1	H_1
Vertical mesh	V_1	V_1	V_1	V_1	V_2	V_3
Temperature profile	T_1	T_1	T_1	T_1	T_1	T_1
Salinity profile	S_1	S_1	S_1	S_1	S_1	S_1
Number of elements	120,000	156,546	88,632	79,854	96,000	192,000

Table 2

Experiments described in Section 6 for different strength in thermal forcing. The variable T_s represents the initial temperature of the deep water, which is the source of melting.

Case	$T_s = 2$ °C	$T_s = 1$ °C	$T_s = 0$ °C	$T_s = -1$ °C	$T_s = -1.8$ °C
Horizontal mesh	H_1	H_1	H_1	H_1	H_1
Vertical mesh	V_1	V_1	V_1	V_1	V_1
Temperature profile	T_2	T_3	T_4	T_5	T_6
Salinity profile	S_2	S_2	S_2	S_2	S_2
Number of elements	120,000	120,000	120,000	120,000	120,000

where T_s and S_s represent the temperature and salinity of the source water that drives the melting, and T_f is the freezing temperature. In our case, one can imagine that the source water is at the ocean end of the ice–ocean boundary layer, and our three-equation melting parameterisation, (5)–(7), is turbulent, steady and one-dimensional. The theory of Gade (1979) holds over the boundary layer, and any meltwater produced will therefore be on the straight line from the source water applied at the ocean end of the boundary layer, described by (10). The “Base case” listed in Table 1 uses a single ‘far-field’ water mass (initialised with constant temperature and salinity). This constant-property water only mixes with its own meltwater; therefore, all the water in the domain follows along the straight line (10) with $T_s = T_1$ and $S_s = S_1$ by construction of the problem setup and melting parameterisation.

The shelf-averaged melt rate is used to diagnose the evolution of the system. This is defined as the integral of the melt rate over the ice shelf’s base, Ω_B , and ice front, Ω_F , normalised by the area of the ice base, A_{Ω_B} , and front A_{Ω_F} :

$$\bar{m}_s = \frac{\int_{\partial\Omega_B} m dA + \int_{\partial\Omega_F} m dA}{A_{\Omega_B} + A_{\Omega_F}}. \quad (11)$$

At the beginning of the simulation, \bar{m}_s rapidly increases then slowly decreases to a steady state (Fig. 4(a)). Melting produces meltwater that is cooler and fresher than the ambient water, so the water in the domain starts to evolve along Eq. (10) from the prescribed constant initial conditions (Fig. 4(b)). The ocean loses the original T_1 and S_1 in steady state, indicating that the meltwater has flushed the ocean (Fig. 4(c)). The properties of all modified water are consistent with the theory of Gade (1979).

The density of water near the freezing point is controlled by salinity rather than temperature, so ice-shelf meltwater is always buoyant relative to its surroundings. In the Southern Hemisphere the Coriolis force acts to steer the rising meltwater to the left, and the high flow speeds associated with this current drive a band of high melt rates on the western side of our domain (Fig. 5(a)). At the ice front, the meltwater rises toward the surface owing to its high buoyancy. The water column becomes stratified by the meltwater (Fig. 5(b)), with the surface occupied by cool, fresh water and the bottom filled with warm water from the northern boundary. As the meltwater hits the northern boundary it sinks to the bottom and circulates toward the grounding line along the eastern boundary (Fig. 5(c)).

4. Different horizontal and vertical meshes

Different horizontal meshes employ different horizontal spatial resolution at the northern boundary, dr (see Fig. 1). All cases have a cyclonic gyre, centred 10 km north of the ice front (Fig. 6(a)–(c)). Because the horizontal resolution at the ice front is kept fixed, the position of the cyclonic gyre and its circulation has the same features in all the cases. In the open ocean, the boundary current thickens from 5 km width at the ice front to 10 km at the northern boundary (Fig. 6(a)). Because of the no-normal-flow condition applied at the northern boundary, the current recirculates back to the ice shelf. As the dr increases, the recirculation near the northern boundary becomes poorly represented (Figs. 6(b) and (c)). Despite this difference, the distribution of the ice-shelf melt rate is nearly identical in all the cases in the absence of surface buoyancy forcing in the open ocean (Figs. 6(a)–(c)). The case with $dr = 1$ km has twice as many elements as in the case with $dr = 10$ km (Table 1), yet the distribution of the melt rate is the same, demonstrating the potential computational benefits of the use of unstructured meshes, given the absence of surface buoyancy forcing in the open ocean. Surface buoyancy forcing plays an important role in driving exchange between the cavity and open ocean, and applying a realistic surface buoyancy forcing could of course change the acceptable range of dr in the open ocean.

The effects of different vertical meshes are not as straightforward. As the number of elements increases in the vertical direction, the shelf-averaged melt rate \bar{m}_s converges toward $\sim 65 \text{ m yr}^{-1}$ (Fig. 7). The quasi- σ coordinate achieves this result for less than half of the number of elements of the quasi- z coordinate (Table 1). In the quasi- z coordinate, decreasing the number of elements in the vertical direction by 50% results in a 10% reduction of the steady-state \bar{m}_s . This difference in \bar{m}_s comes from the distribution of m near the grounding line (Fig. 7(a)). Decreasing the vertical spacing by half tends to align the melt rate contours in the north-south direction and pushes the contours toward the east (Fig. 7(c) and (d)). The eastward spread of the contours is pronounced in the σ case near the grounding line, as the vertical resolution gets finer towards the south (Fig. 7(b)).

5. Different domain geometry

All ocean models that have previously been adapted to model ice shelf cavities require the application of a minimum water-column thickness to prevent the breakdown of their assumptions; none can smoothly collapse the vertical layer at the grounding line to a singular point. This could be problematic in some cases, as

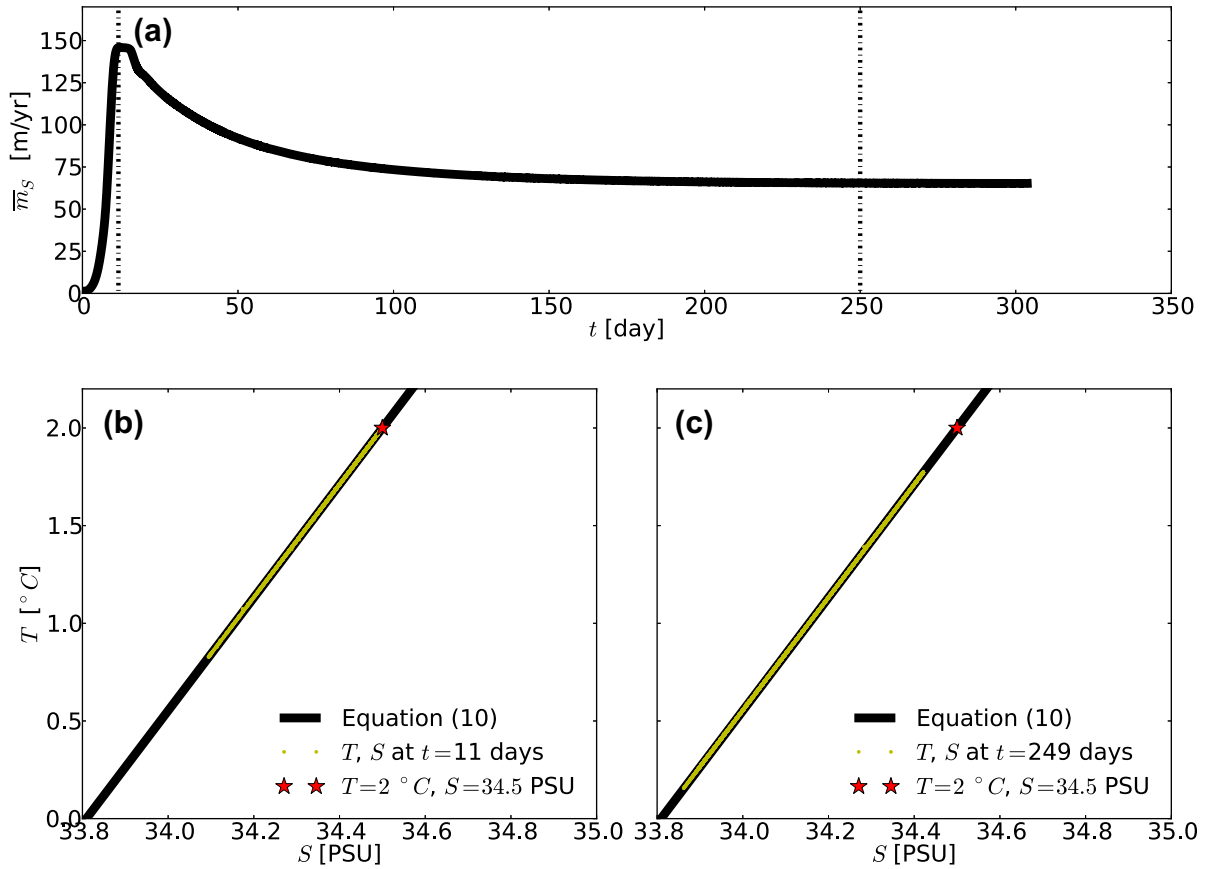


Fig. 4. (a) Evolution of \bar{m}_s from the base case. Two dashed lines indicate the time when the snapshots in (b) and (c) are taken. Temperature and salinity relationship of the base case and the (10) at $t = 34$ (a) and $t = 249$ (b) days. The source water melts the ice, modifying the temperature and salinity along Eq. (10). After 249 days, all the source water has been modified to the meltwater.

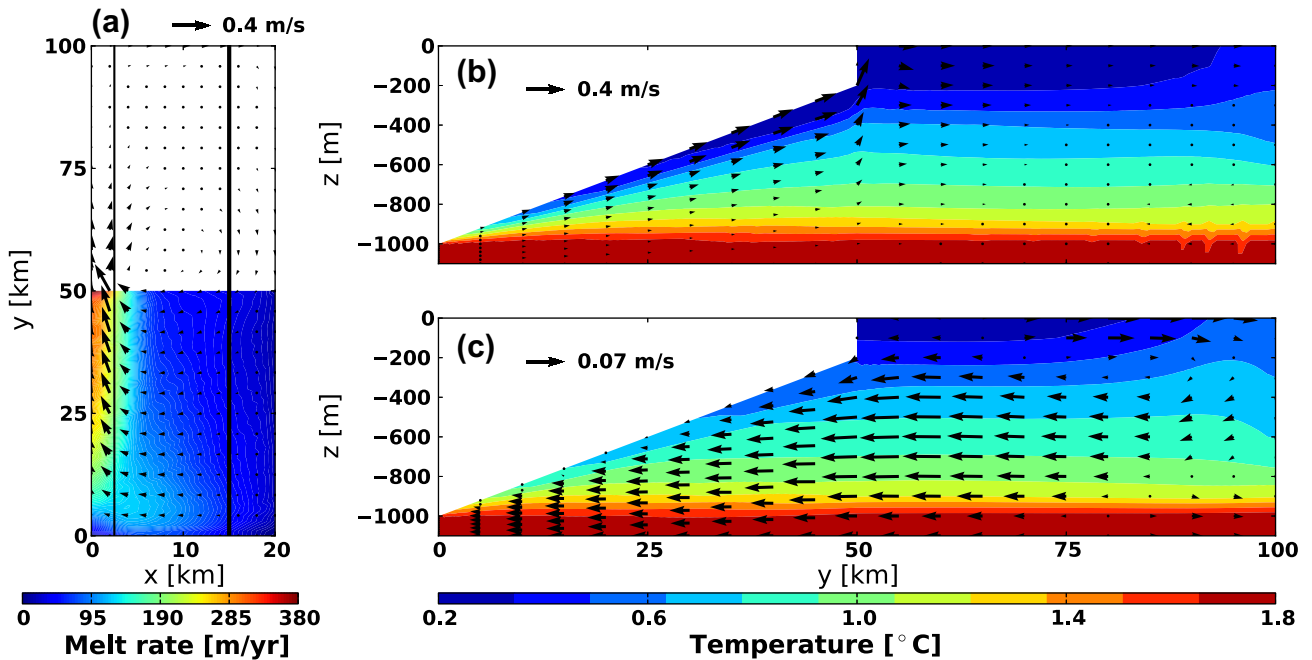


Fig. 5. (a) Snapshot of melt rate (colour coded) and velocity vectors, u and v , along the layer that contains the ice base at $t = 249$ days. The thin and thick solid lines indicate the meridional transect plots shown in (b) and (c), respectively. (b) Meridional transect of temperature (colour coded) and velocity vectors, v and w at $x = 2.5$ km. (c) Meridional transect of temperature (colour coded) and velocity vectors, v and w at $x = 15$ km. Velocity vectors are sub-sampled onto a regular grid.

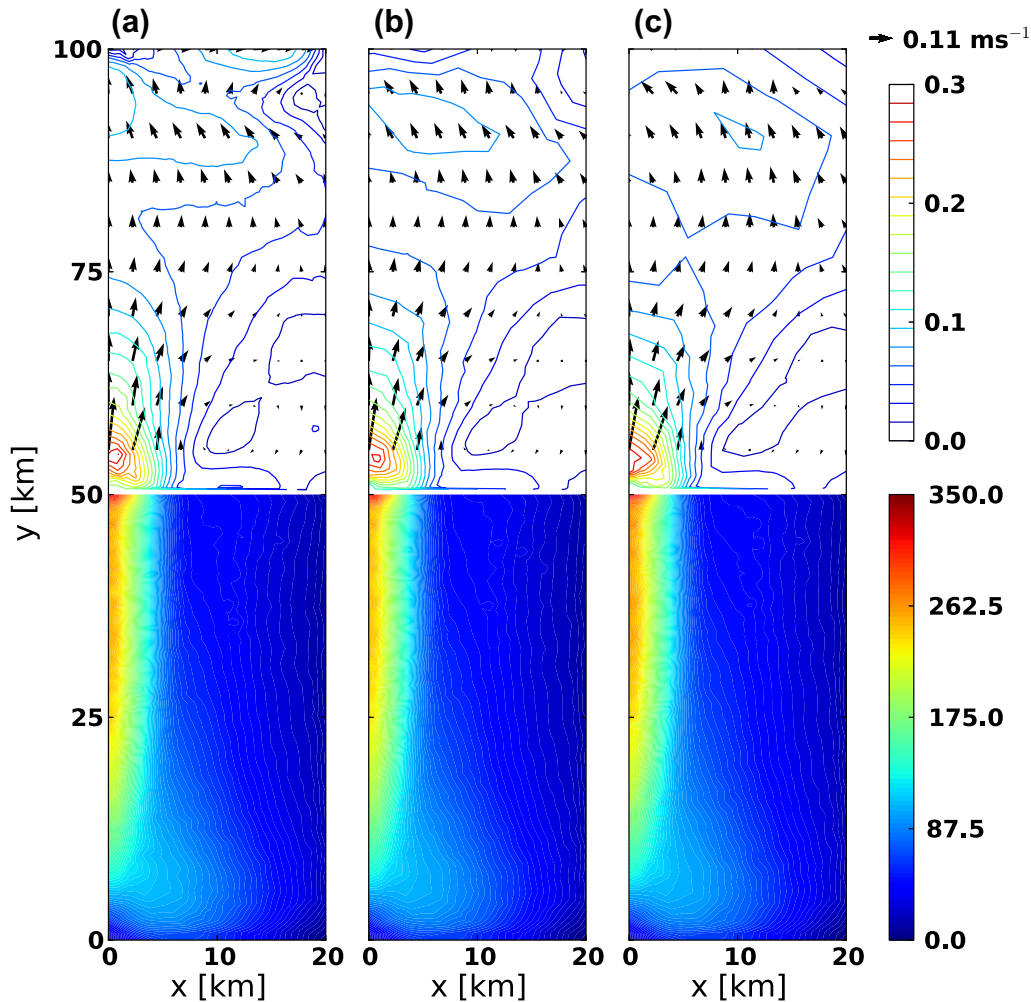


Fig. 6. Melt rate along the ice base ($0 \leq y \leq 50$ km) and the circulation of the open-ocean ($50 \leq y \leq 100$ km) at the surface layer, for different horizontal meshes: (a) $dr = 1$ km; (b) $dr = 5$ km; (c) $dr = 10$ km. The horizontal and vertical meshes that are used in these simulations are listed in Table 1. Circulations of the open ocean are indicated by the contours of horizontal speed and selected horizontal velocity vectors. As dr increases, the velocity vectors near the Northern boundary lose the streamwise variations due to the coarsening of the resolution.

ocean processes near the grounding line, where the ice transitions from floating to grounded, can be important (Holland, 2008; Jenkins, 2011). The use of an unstructured mesh and finite elements removes this constraint; we could allocate one or more triangular elements exactly at the grounding line, as demonstrated by one of our quasi- σ coordinate cases (Fig. 2(a)). We find that in our idealised situation this has very little effect on the overall melt rate (Fig. 8(a)). The amount of warm deep water that penetrates near the grounding line is larger and therefore the surface is 0.1 °C warmer in the base case than the grounded case (Fig. 9(b) and (c)), but this is not significant enough to change the evolution of \bar{m}_S in the range of spatial resolution that we used. However, it is possible that the introduction of a more realistic environment, including the effects of tides and sub-glacial meltwater (Holland, 2008; Jenkins, 2011), would benefit significantly from this ability.

Accurately representing the vertical ice front in σ -coordinate models is difficult due to horizontal pressure gradient errors, and a typical solution is to smooth the vertical ice face into a steep basal ice slope (Beckmann et al., 1999; Dinniman et al., 2007). We now consider cases with the removal and smoothing a vertical ice front. The vertical ice front is simply removed in the model by extending the slope of the ice base up to the open-ocean surface (Fig. 9(a)). The smoothing of the ice front is designed to maintain the area of ice–ocean interface by tilting the vertical ice front

around the mid-depth ($z = -100$ m) of the vertical ice front, i.e., the total area of the ice–ocean interface is maintained by reducing the area of the ice-base (Fig. 9(b)).

The removal of the ice front is found to lower \bar{m}_S (Fig. 8(a)). However, because the area of the ice shelf–ocean interface has increased, this does not imply a reduction in heat and salt fluxes to the ocean. The area of vertical ice front in the base case is 4.0×10^6 m², while the removed portion of the vertical ice front contains 2.4×10^8 m² of ice facing the ocean. To account for this difference in the area, we define integrated melt rates over the area of the ice base, m_B , and vertical ice front, m_F :

$$m_B = \int_{\partial\Omega_B} m ds, \quad m_F = \int_{\partial\Omega_F} m ds. \quad (12)$$

Because the steepness and the area of the ice base are the same between the vertical and removed ice front cases, m_B evolves the same way. The reduction of the ice base area in the smoothed ice front case is not significant enough to change the evolution of m_B (Fig. 8(b)). The difference of two orders of magnitude in the area of ice–ocean interface between the vertical and removed ice front cases is reflected in the evolution of m_F . When the ice-covered area is maintained, the m_F is slightly higher than the base case. Even though the area of the ice is kept the same, the integrated input of meltwater is higher, cooling and freshening the ocean more than

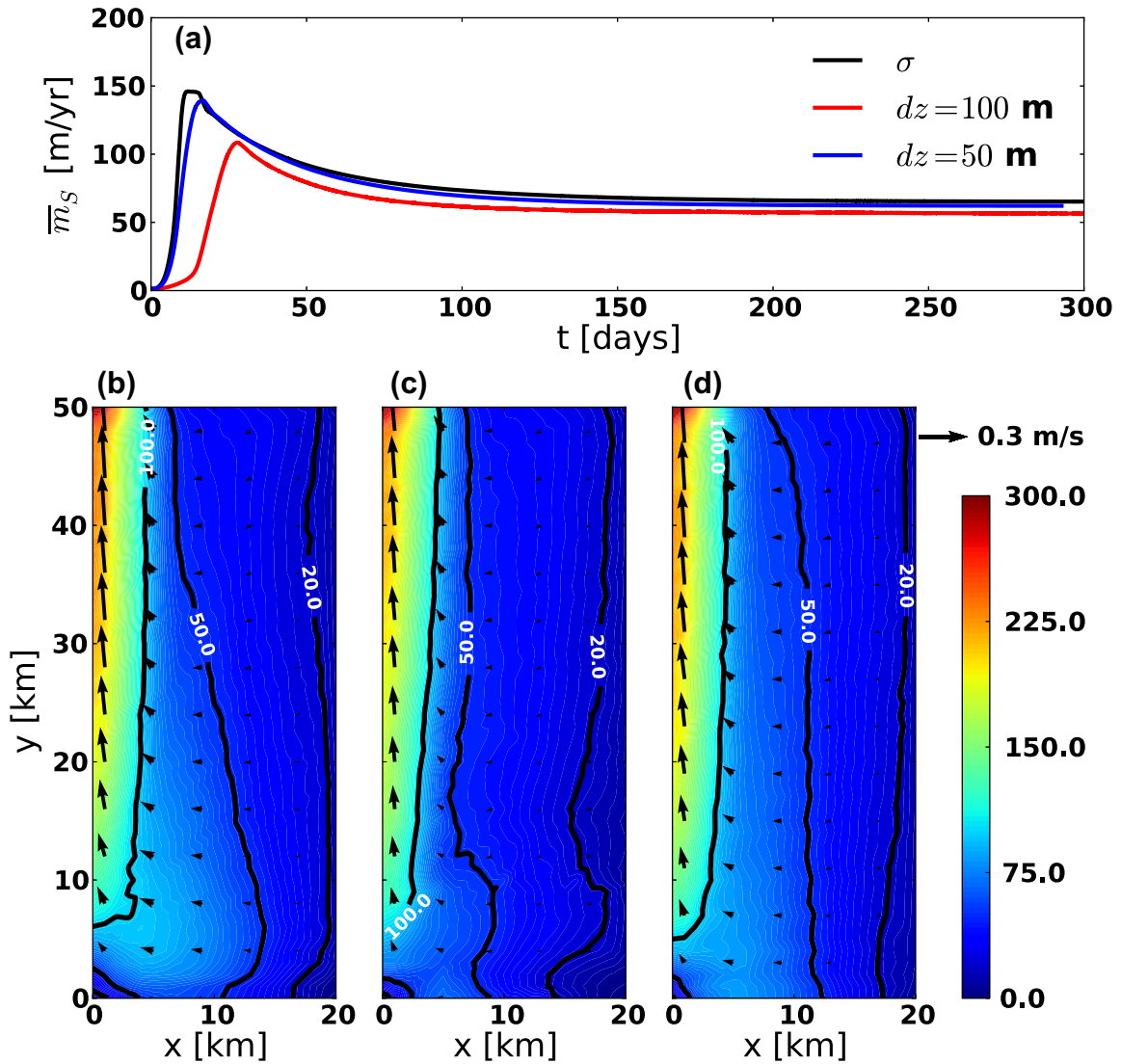


Fig. 7. Evolutions of \bar{m}_s [m/yr] for different vertical meshes (a). Distribution of the melt rate along the ice base at $t = 200$ days: (b) σ ; (c) $dz = 100$ m; (d) $dz = 50$ m. The melt rate is colour coded and the dark contours indicate selected values of melt rates. The arrows represent the velocity u and v along the ice base.

the vertical ice front case (Fig. 8(c)). This is due to the accelerated flow along the smoothed ice front, producing more meltwater relative to the base case (Fig. 9(b)). The meltwater, advected to the surface of the ocean, is substantially cooler in the removed and smoothed ice front cases (Fig. 9(a) and (b)) than the other two cases, which contain the vertical ice front (Fig. 9(c) and (d)).

6. Different thermal forcing

The study of Holland et al. (2008b) used an isopycnal-coordinate ocean model in an idealised ice-shelf cavity domain to show that ice shelf melting increases as the water offshore is warmed. The increase was found to be above-linear (quadratic); the warming increases the heat available for melting, and also increases the flow speed of the meltwater layer, mixing proportionately more heat towards the ice shelf. We now revisit this test to ensure that the results apply in a smaller domain, more representative of the ice shelves of current interest, and with a model that contains a more general treatment of the ocean. We employ the same temperature and salinity profiles of Holland et al. (2008b) but use our smaller domain, with a 50 km ice shelf rather than the 500 km used by Holland et al. (2008b).

As the meltwater flushes the ice shelf cavity, the \bar{m}_s finds its equilibrium with the restoring conditions at the northern boundary. The response of shelf-averaged melt rate to the variations in T_S is non-linear (Fig. 10(a)), as reported for larger ice shelves by Holland et al. (2008b). The thermal forcing strongly influences the outflow of the melt water (Fig. 10(b)–(d)). In all cases, a band of higher melting is concentrated at the western boundary. As the thermal forcing decreases, the magnitude of the ascending flow decreases and the location of the maximum melt rate descends toward the grounding line region. In the $T_S = 2^\circ\text{C}$ and $T_S = 0^\circ\text{C}$ cases, the meltwater ascends up to the ice front. This outflow process cools the water inside the ice shelf cavity (Fig. 10(b) and (c)). In contrast, the rising melt water separates from the ice shelf in the $T_S = -1^\circ\text{C}$ case, as it has reached neutral buoyancy relative to the stratified surroundings. In this case, the ambient water of -1°C floods into the cavity near the ice front (Fig. 10(d)). This behaviour was not found in the study of Holland et al. (2008b). This could be because the ice shelf was more gently sloping in that case, or it could be that the isopycnal model used relied upon a mixed-layer parameterisation that was unable to properly represent the separation. Unlike simulations of large ice shelves, such as Holland et al. (2008b), the model does not produce any freezing along the

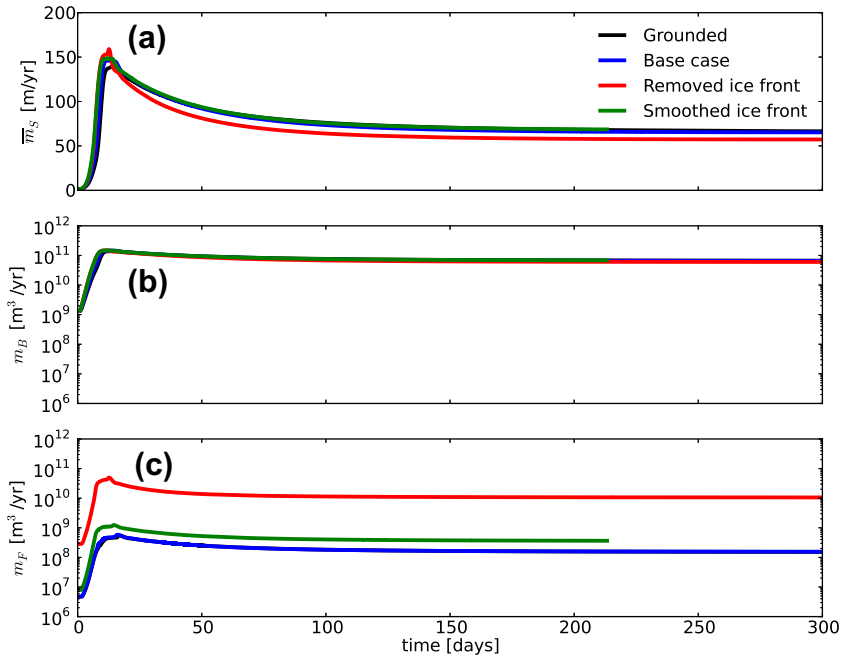


Fig. 8. Evolution of (a) \bar{m}_s , (b) m_B and (c) m_F for different ice-shelf geometry.

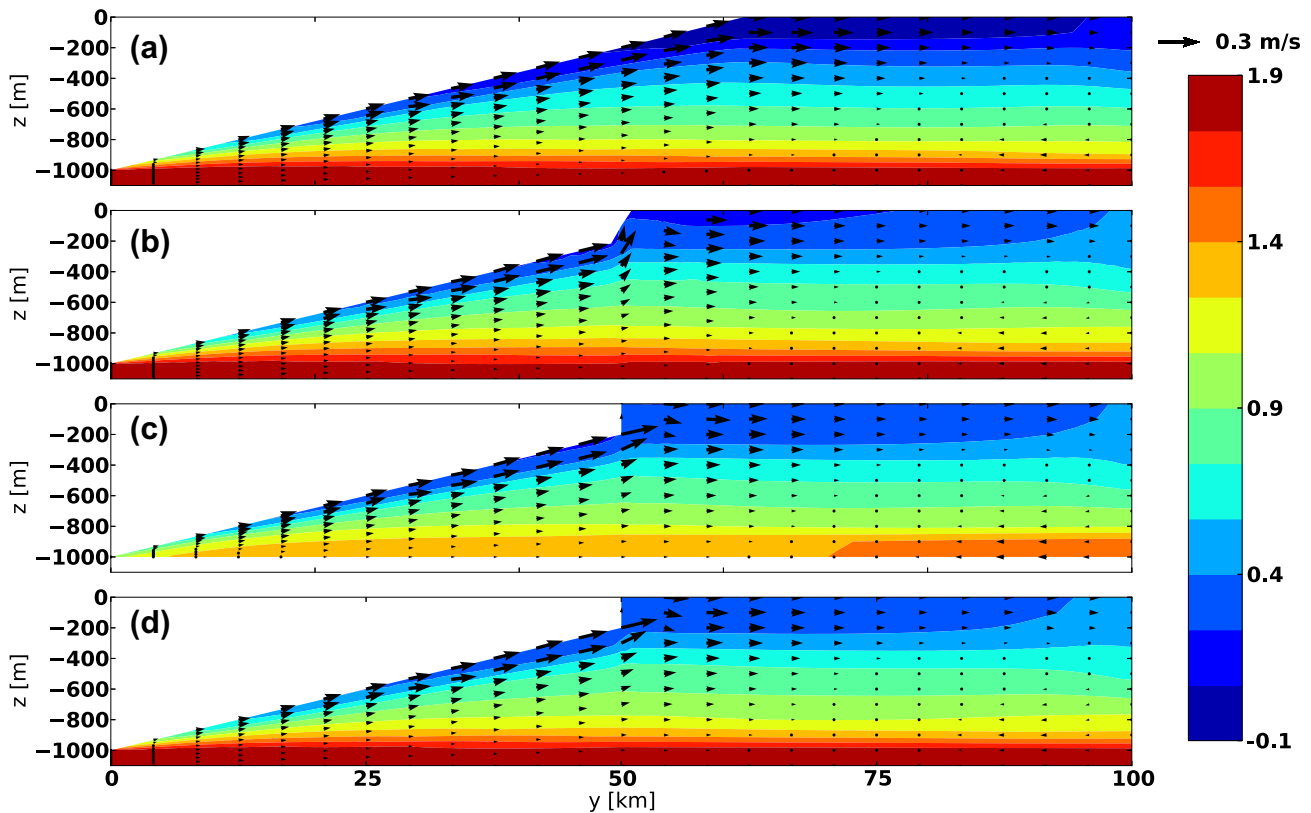


Fig. 9. Snapshots of temperature and velocity fields (v and w) along $x = 3$ km at $t = 185$ days: (a) removed ice front, (b) smoothed ice front, (c) grounded and (d) base cases.

ice base. In smaller, steeper ice shelves forced by warm water, such as that modelled here, the ice-shelf meltwater mixes with too much warm water to produce freezing. This faster flow along the ice base means that the melt rate is higher than the large ice shelves. The least-square fit of the melt rate with respect to T_S to a second polynomial gives $m = 2.5T_S^2 + 12.5T_S + 13.3$ with

$R^2 = 0.99$, where Holland et al. (2008b) result indicate $m = 0.341T_S^2 + 2.365T_S + 3.003$ with $R^2 = 0.95$. As shown by Holland et al. (2008b), smaller, steeper ice shelves have higher melt rate for a given thermal forcing than large ice shelves so that a single melting curve for all ice shelves does not exist.

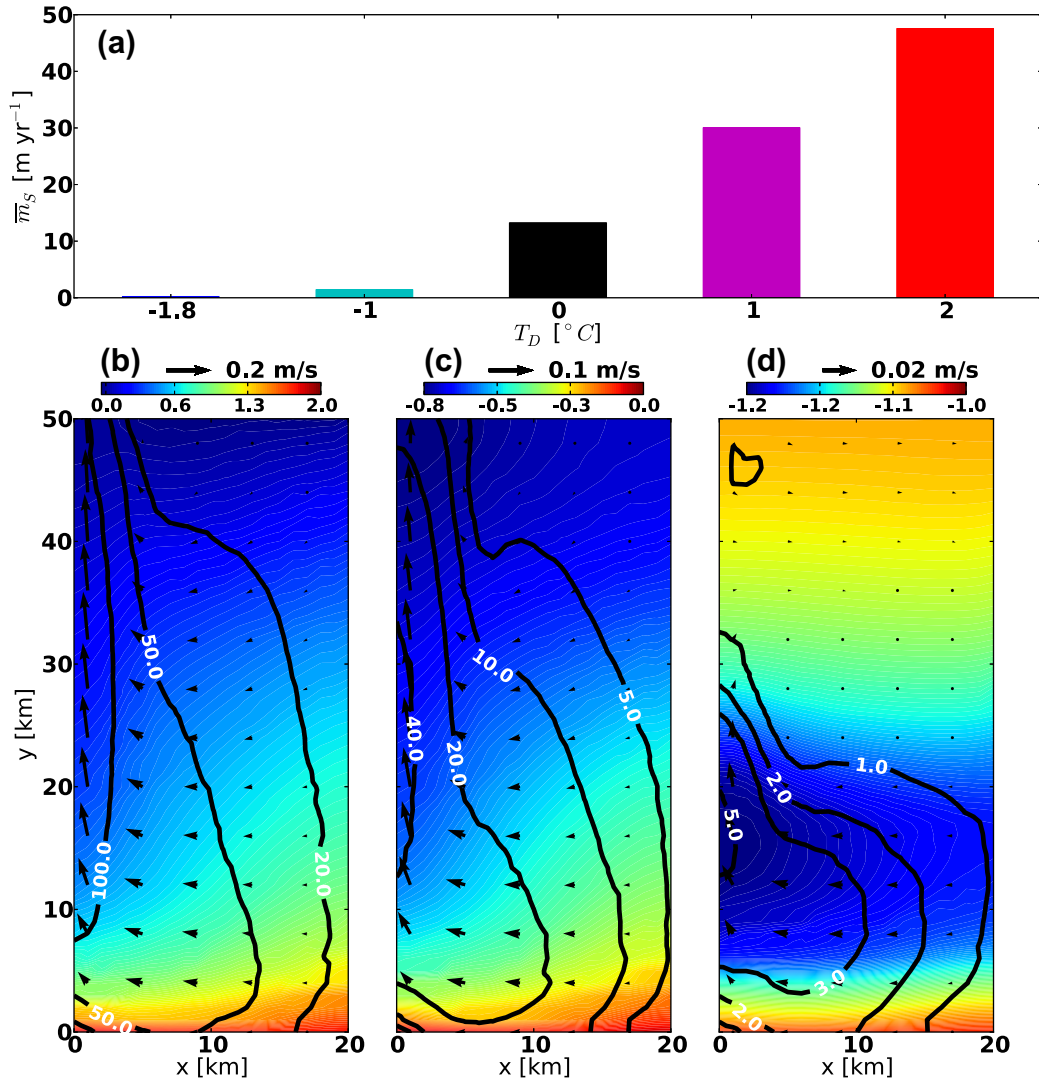


Fig. 10. (a) Steady-state \bar{m}_S averaged over time between 200 and 300 days with respect to different T_S . Snapshots of melt rate along the ice base after 260 days: (b) $T_S = 2^{\circ}\text{C}$; (c) $T_S = 0^{\circ}\text{C}$ and (d) -1°C . The colours represent the temperature and the contours indicate the selected melt rates in m yr^{-1} . The arrows indicate u and v that were used to calculate the melt rate.

The meltwater is light enough to ascend up to the surface of the open ocean in the $T_S = 2^{\circ}\text{C}$ case (Fig. 11(a) and (b)). The isopycnals along the ice base are pushed toward the surface layer and the ascended melt water occupies the upper layer. The initial surface water of -1.8°C is replaced by the warmer meltwater; the surface of the ocean is warmed by the ascending meltwater. The ascending flow is the fastest at the Western boundary (Figs. 10(b) and 11(a)). The ascending flow slows down away from the Western boundary. At the Eastern part of the domain, the return flow from the Northern boundary brings the warm water ($T = 2^{\circ}\text{C}$) to the grounding line regions (Fig. 11(b)).

In the lower forcing temperature, $T_S = -1^{\circ}\text{C}$, the meltwater is denser than the water mass specified near the ocean surface. Unlike the $T_S = 2^{\circ}\text{C}$ case, the water mass near the ocean surface is virtually unaffected by the meltwater (Fig. 11(c)). The pycnocline below the surface layer prevents the meltwater from rising to the surface. The plume of meltwater detaches from the ice base at the middle of the ice shelf cavity (Fig. 11(c)). This detached meltwater intrudes into the open ocean, cooling the deep water inside the cavity and the open ocean. The return flow at the bottom from

the open ocean brings the water from the Northern boundary toward the grounding line region to further melt the ice (Fig. 11(c)).

7. Conclusions

We have presented some results from the implementation of floating glacial ice shelves into the nonhydrostatic, unstructured-mesh, finite-element ocean model Fluidity-ICOM. We have examined the effect of various choices for the vertical and horizontal mesh, and details of the domain geometry and ocean forcing.

1. In our idealised experiments with no forcing on the open ocean, changing the horizontal resolution by an order of magnitude in the ocean outside the ice-shelf cavity does not affect the distribution of the melt rate as long as the horizontal resolution inside the ice shelf cavity is kept the same. In contrast, a lack of vertical resolution near the grounding line can underestimate the melt rate. This clearly demonstrates the potential efficiencies of the ability to focus computational resolution in desired locations.

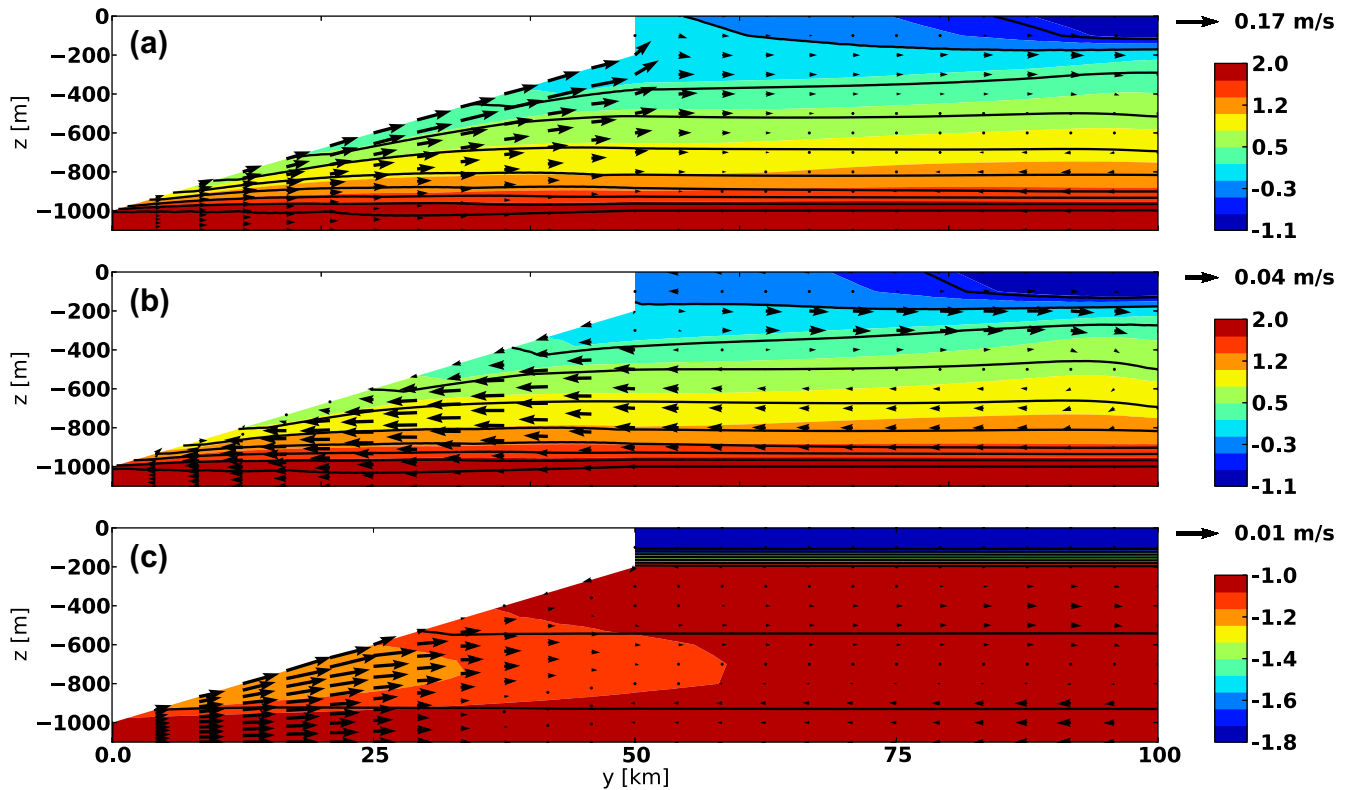


Fig. 11. Snapshots of temperature (colour coded) and velocity vectors (v and w) at $t = 200$ days. Meridional transects from $T_S = 2$ °C case at (a) $x = 2.5$ km and (b) $x = 10$ km. Meridional transect from $T_S = -1$ °C case at (c) $x = 2.5$ km. The solid contours represent isopycnals. Arrows indicate the velocity vectors, v and w .

2. The amount of warm water that penetrates beneath the cavity is larger, enabling the presence of slightly warmer surface water, in the case of the finite water-column thickness case than the zero water-column thickness grounding lines. However, this warming of the surface is small enough that the evolution of shelf-averaged melt rate does not change.
3. The increase in the area of ice–ocean interface by the removal of a vertical ice front does not affect the mean melt rate but does enhance the integrated input of meltwater to the ocean. When the smoothing of the ice front is designed to maintain the area of ice–ocean interface, the flow along the smoothed ice front accelerates and increases the integrated input of meltwater, cooling and freshening the ocean more than the vertical ice front case. Our ability to represent melting or freezing on ice faces oriented in any direction has great potential for application to vertical ice faces, for example in Greenland fjords.
4. As found in previous studies, the melt rate increases non-linearly as the temperature of the water forcing the cavity increases. However, the model is able to represent the dynamics of a meltwater plume that separates from the ice shelf when it reaches neutral buoyancy, unlike previous models with mixed-layer parameterisation. In the warmest case, the meltwater is lighter than the surrounding water, thereby warming the surface of the ocean. As the deep water temperature decreases, the meltwater is not light enough to penetrate to the surface, so it intrudes into the open ocean, cooling the deep water.

The capabilities of this model clearly have great potential for the future, and the results presented here are only a first step. In particular, our next steps are to fully implement the pressure loading of the floating ice shelf with the capability to adapt mesh, and to apply the model to the complex ice-shelf and fjord topography in which its capabilities will prove essential.

Acknowledgements

Comments from one anonymous reviewer and Xylar Asay-Davis improved the manuscript. The work was supported by the UK Natural Environment Research Council under grants NE/G018391/1 and NE/G018146/1.

References

- Adcroft, A., Hill, C., Marshall, J., 1997. Representation of topography by shaved cells in a height coordinate ocean model. *Mon. Weather Rev.* 125 (9), 269–284.
- Beckmann, A., Hellmer, H.H., Timmermann, R., 1999. A numerical model of the Weddell sea: large-scale circulation and water mass distribution. *J. Geophys. Res.* 104, 23375–23392.
- Cotter, C.J., Ham, D.A., Pain, C.C., Reich, S., 2009. LBB stability of a mixed Galerkin finite element pair for fluid flow simulations. *J. Comput. Phys.* 228 (2), 336–348.
- Danilov, S., Kivman, G., Schröter, J., 2004. A finite-element ocean model: principles and evaluation. *Ocean Modell.* 6, 125–150.
- Determann, J., Gerdes, R., 1994. Melting and freezing beneath ice shelves: implications from a three-dimensional ocean-circulation model. *Ann. Glaciol.* 20, 413–419.
- Dinniman, M.S., Klinck, J.M., Smith Jr, W.O., 2007. Influence of sea ice cover and icebergs on circulation and water mass formation in a numerical circulation model of the Ross Sea. *J. Geophys. Res.* 112, C11013. <http://dx.doi.org/10.1029/2006JC004036>.
- Gade, H.G., 1979. Melting of ice in sea water: a primitive model with application to the Antarctic ice shelf and icebergs. *J. Phys. Oceanogr.* 9, 189–198.
- Gary, J.M., 1973. Estimate of truncation error in transformed coordinate primitive equation atmospheric models. *J. Atmos. Sci.* 30, 223–233.
- Geuzaine, C., Remacle, J.F., 2009. Gmsh: a three-dimensional finite element mesh generator with built-in pre- and post-processing facilities. *Int. J. Numer. Methods Eng.* 11, 1309–1331.
- Grosfeld, K., Gerdes, R., Determann, J., 1997. Thermohaline circulation and interaction between ice shelf cavities and the adjacent open ocean. *J. Geophys. Res.* 102, 15595–15610.
- Haney, R.L., 1991. On the pressure gradient force over steep topography in sigma coordinate ocean models. *J. Phys. Oceanogr.* 21, 610–619.
- Hellmer, H., Olbers, D., 1989. A two-dimensional model for the thermohaline circulation under an ice shelf. *Antarct. Sci.* 1, 325–336.

- Holland, D.M., Jenkins, A., 1999. Modeling thermodynamic iceocean interactions at the base of an ice shelf. *J. Phys. Oceanogr.* 29, 1787–1800.
- Holland, D.M., Jenkins, A., 2001. Adaptation of an isopycnic coordinate ocean model for the study of circulation beneath ice shelves. *Mon. Weather Rev.* 129, 1905–1927.
- Holland, D.M., Thomas, R.H., Young, B.D., Ribergaard, M.H., Lyberth, B., 2008a. Acceleration of Jakobshavn Isbrae triggered by warm subsurface ocean waters. *Nat. Geosci.* 1, 659–664.
- Holland, P.R., 2008. A model of tidally dominated ocean processes near ice shelf grounding lines. *J. Geophys. Res.* 113, C11002.
- Holland, P.R., Feltham, D.L., 2006. The effects of rotation and ice shelf topography on Frazil–Laden ice shelf water plumes. *J. Phys. Oceanogr.* 36, 2312–2327.
- Holland, P.R., Jenkins, A., Holland, D.M., 2008b. The response of ice shelf basal melting to variations in ocean temperature. *J. Clim.* 21, 2558–2572.
- Jacobs, S.S., Gordon, A.L., Ardai, J.L., 1979. Circulation and melting beneath the Ross ice shelf. *Science* 203, 439–442.
- Jacobs, S.S., Helmer, H.H., Doake, C., Jenkins, A., Frolich, R.M., 1992. Melting of ice shelves and the mass balance of Antarctica. *J. Glaciol.* 38, 375–387.
- Jacobs, S.S., Helmer, H.H., Jenkins, A., 1996. Antarctic ice sheet melting in the Southeast Pacific. *J. Geophys. Res.* 23, 957–960.
- Jenkins, A., 1999. The impact of melting ice on ocean waters. *J. Phys. Oceanogr.* 29, 2370–2381.
- Jenkins, A., 2011. Convection-driven melting near the grounding lines of ice shelves and tidewater glaciers. *J. Phys. Oceanogr.* 41, 2279–2294.
- Jenkins, A., Bombosch, A., 1995. Modeling the effects of frazil ice crystals on the dynamics and thermodynamics of ice shelf water plumes. *J. Geophys. Res.* 100, 6967–6981.
- Jenkins, A., Dutrieux, P., Jacobs, S.S., McPhail, S.D., Perrett, J.R., Webb, A.T., White, D., 2010. Observations beneath Pine island glacier in West Antarctica and implications for its retreat. *Nat. Geosci.* 3, 468–472.
- Jenkins, A., Hellmer, H., Holland, D., 2001. The role of meltwater advection in the formulation of conservative boundary conditions at an ice–ocean interface. *J. Phys. Oceanogr.* 31, 285–296.
- Jenkins, A., Holland, D., 2002. A model study of ocean circulation beneath Filchner–Ronne ice shelf, Antarctica: implications for bottom water formation. *Geophys. Res. Lett.* 29, 1193.
- Jenkins, A., Vaughan, D.G., Jacobs, S.S., Hellmer, H.H., Keys, J.R., 1997. Glaciological and oceanographic evidence of high melt rates beneath Pine island glacier, West Antarctica. *J. Glaciol.* 43, 114–121.
- Kramer, S.C., Cotter, C.J., Pain, C.C., 2009. Solving the poisson equation on small aspect ratio domains using unstructured meshes. *Ocean Modell.* 35, 253–263.
- Little, C., Gnanadesikan, A., Hallberg, R., 2008. Large-scale oceanographic constraints on the distribution of melting and freezing under ice shelves. *J. Phys. Oceanogr.* 38 (10), 2242–2255.
- Losch, M., 2008. Modeling ice shelf cavities in a z-coordinate ocean general circulation model. *J. Geophys. Res.* 113, C08043.
- Lynch, D.R., Ip, J., Naimie, C.E., Werner, F.E., 1996. Comprehensive coastal circulation model with application to the Gulf of Maine. *Cont. Shelf Res.* 16, 875–906.
- MacAyeal, D.R., 1984. Thermohaline circulation below the Ross ice shelf: a consequence of tidally induced vertical mixing and basal melting. *J. Geophys. Res.* 89, 597–606.
- Makinson, K., Holland, P.R., Jenkins, A., Nicholls, K.W., Holland, D.M., 2011. Influence of tides on melting and freezing beneath Filchner–Ronne ice shelf, Antarctica. *Geophys. Res. Lett.* 38, L06601.
- McDougall, T., Jackett, D., Wright, D., Feistel, R., 2003. Accurate and computationally efficient algorithms for potential temperature and density of seawater. *J. Atmos. Oceanic Technol.* 20, 730–741.
- McPhee, M.G., 2008. *Air–Ice–Ocean Interaction*. Springer.
- Mellor, G.L., Ezer, T., Oey, L.Y., 1994. The pressure gradient conundrum of sigma coordinate ocean models. *J. Atmos. Oceanic Technol.* 11, 1126–1134.
- Nicholls, K.W., Østerhus, S., 2004. Interannual variability and ventilation timescales in the ocean cavity beneath Filchner–Ronne ice shelf, Antarctica. *J. Geophys. Res.* 109, C04014. <http://dx.doi.org/10.1029/2003JC002149>.
- Nicholls, K.W., Østerhus, S., Makinson, K., Gammelsrød, T., Fahrbach, E., 2009. Ice-ocean processes over the continental shelf of the Southern Weddell sea, Antarctica: a review. *Rev. Geophys.* 49, RG4001. <http://dx.doi.org/10.1029/2007RG000250>.
- Piggott, M.D., Gorman, G.J., Pain, C.C., Allison, P.A., Candy, A.S., Martin, B.T., Wells, M.R., 2008. A new computational framework for multi-scale ocean modelling based on adapting unstructured meshes. *Int. J. Numer. Methods Fluids* 56, 1003–1015.
- Pritchard, H.D., Arthern, R.J., Vaughan, D.G., Edwards, L.A., 2009. Extensive dynamic thinning on the margins of the Greenland and Antarctic ice sheets. *Nature* 461, 971–975.
- Rignot, E., Kanagaratham, P., 2006. Changes in the velocity structure of the Greenland ice sheet. *Science* 311, 986–990.
- Rignot, E., Steffen, P., 2008. Channelized bottom melting and stability of floating ice shelves. *Geophys. Res. Lett.* 35, L02503.
- Shepherd, A., Wingham, D., Rignot, E., 2004. Warm ocean is eroding West Antarctic ice sheet. *Geophys. Res. Lett.* 31, L23402.
- Smethie, W.M., Jacobs, S., 2005. Circulation and melting under the Ross ice shelf: estimates from evolving CFC, salinity and temperature fields in the Ross sea. *Deep Sea Res.* 52, 959–978.
- Steig, E.J., Ding, Q., Battisti, D., Jenkins, A., 2012. Tropical forcing of circumpolar deep water inflow and outlet glacier thinning in the Amundsen sea embayment, West Antarctica. *Ann. Glaciol.* 53, 19–28.
- Straneo, F., Hamilton, G., Sutherland, D., Stearns, L.A., Davidson, F., Hammill, M.O., Stenson, G.B., Rosing-Asvid, A., 2010. Rapid circulation of warm subtropical waters in a major glacial Fjord in East Greenland. *Nat. Geosci.* <http://dx.doi.org/10.1038/NGE0764>.
- Thoma, M., Jenkins, A., Holland, D., Jacobs, S., 2008. Modelling circumpolar deep water intrusions on the Amundsen Sea continental shelf, Antarctica. *Geophys. Res. Lett.* 35 (18), L18602. <http://dx.doi.org/10.1029/2008GL034939>.
- Timmermann, R., Danilov, S., Schröter, J., Böning, C., Sidorenko, D., Rollenhagen, K., 2009. Ocean circulation and sea ice distribution in a finite element global sea iceocean model. *Ocean Modell.* 27, 114–129.
- Timmermann, R., Wang, Q., Hellmer, H., 2012. Ice-shelf basal melting in a global finite-element sea-ice/ice-shelf/ocean model. *Ann. Glaciol.* 53 (60), 303–314.
- Velicogna, I., 2009. Increasing rates of ice mass loss from the Greenland and Antarctic ice sheets revealed by GRACE. *Geophys. Res. Lett.* 36, L19503.
- Williams, M.J.M., Warner, R., Budd, W., 1998. The effects of ocean warming on melting and ocean circulation under the Amery ice shelf, East Antarctica. *Ann. Glaciol.* 27, 75–80.